nature physics

SUPPLEMENTARY INFORMATION
https://doi.org/10.1038/s41567-018-0334-2

In the format provided by the authors and unedited.

Universal *T*-linear resistivity and Planckian dissipation in overdoped cuprates

A. Legros[1,2], S. Benhabib[3], W. Tabis[3,4], F. Laliberté[1], M. Dion[1], M. Lizaire[1], B. Vignolle[3], D. Vignolles[3], H. Raffy[5], Z. Z. Li[5], P. Auban-Senzier[5], N. Doiron-Leyraud[1], P. Fournier[1,6], D. Colson[2], L. Taillefer[1,6]* and C. Proust[3,6]*

[1]Institut Quantique, Département de Physique & RQMP, Université de Sherbrooke, Sherbrooke, Québec, Canada. [2]SPEC, CEA, CNRS-UMR 3680, Université Paris-Saclay, Gif sur Yvette Cedex, France. [3]Laboratoire National des Champs Magnétiques Intenses (CNRS, EMFL, INSA, UJF, UPS), Toulouse, France. [4]AGH University of Science and Technology, Faculty of Physics and Applied Computer Science, Krakow, Poland. [5]Laboratoire de Physique des Solides, Université Paris-Sud, Université Paris-Saclay, CNRS UMR 8502, Orsay, France. [6]Canadian Institute for Advanced Research, Toronto, Ontario, Canada. *e-mail: louis.taillefer@usherbrooke.ca; cyril.proust@lncmi.cnrs.fr

SUPPLEMENTARY INFORMATION

Universal *T*-linear resistivity and Planckian dissipation in overdoped cuprates

A. Legros *et al*.

CONTENTS

Section 1 – Fermi surfaces (Fig. S1)

Section 2 – Phase diagrams (Fig. S2)

Section 3 – Magneto-resistance (Fig. S3)

Section 4 – *T*-linear resistivity in Nd-LSCO under pressure (Fig. S4)

Section 5 – *T*-linear resistivity in PCCO at H = 0 and H = 16 T (Fig. S5)

Section 6 – *T*-linear resistivity in LCCO at H = 0 (Fig. S6)

Section 7 – *T*-linear resistivity in LSCO (Fig. S7)

Section 8 – Specific heat and Raman intensity in Bi2212 (Fig. S8)

Section 9 – Planckian limit in the organic conductor $(TMTSF)_2PF_6$

Section 10 – Planckian limit in the single-layer cuprate Bi2201

Section 11 – Scaling between magnetic field and temperature in Bi2212 (Fig. S9)

Section 12 – Temperature range of *T*-linear resistivity (Fig. S10)

Section 13 – Tables S1, S2, S3 and S4

Supplementary references – refs. 44-54

Section 1

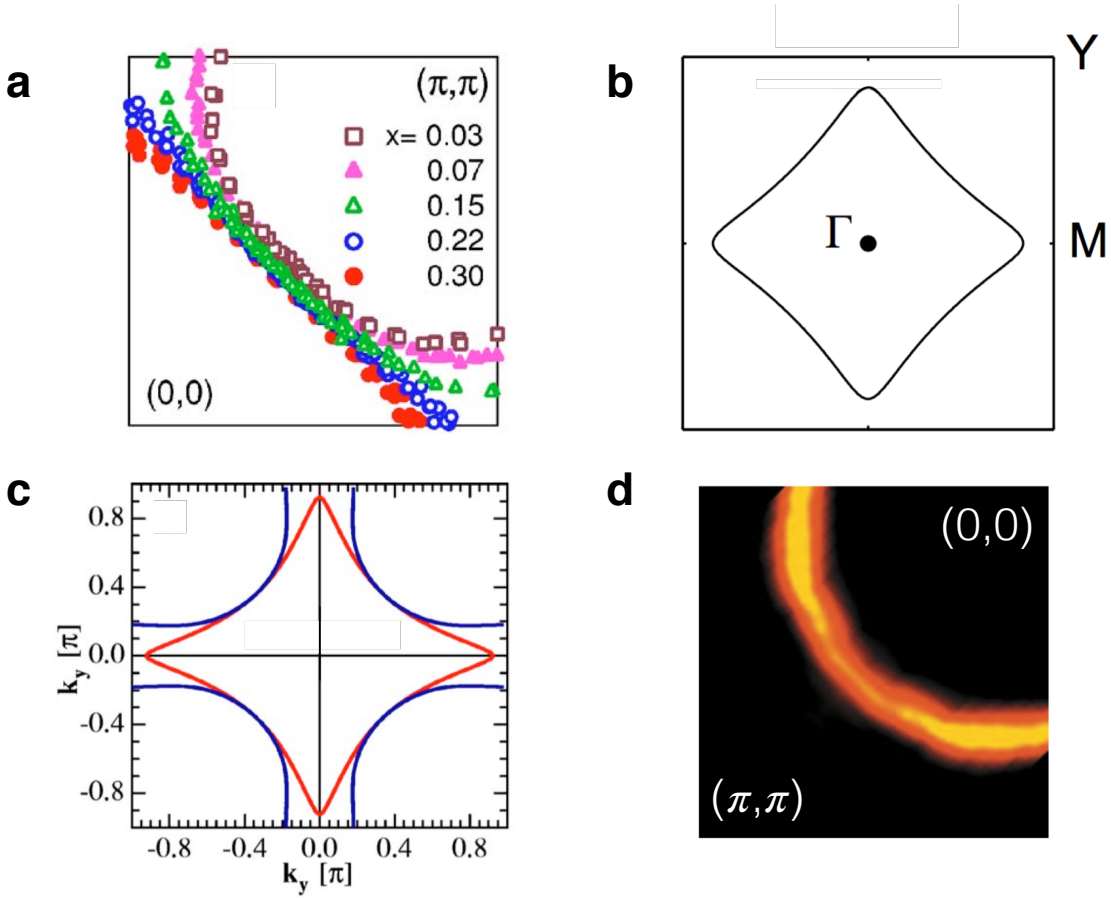

Figure S1 | Fermi surface of the four cuprates.

Fermi surface of four different cuprates, as measured by ARPES: **a)** LSCO at four dopings as indicated (from ref. 20); **b)** Nd-LSCO at p = 0.24 (from ref. 19); **c)** Bi2212 at p = 0.23 (from ref. 21); **d)** NCCO at x = 0.17 (from ref. 28). Note that all are single-layer materials and so have only a single Fermi surface, except for Bi2212, which is a bi-layer material, with two Fermi surfaces, one of which is hole-like (blue), the other electron-like (red).

The Fermi surface area of NCCO (Fig. S1d) is known precisely from the frequency F of quantum oscillations. For the following nominal x values, the following values of F and associated m^* were measured [44]: x = 0.15, 0.16, 0.165, 0.17; F = 10.96 ± 50, 11.10 ± 50, 11.17 ± 100, 11.25 ± 100 kT; m^* = 3.0 ± 0.3, 2.7 ± 0.1, 2.5 ± 0.1, 2.3 ± 0.05. The precise values of x obtained from the measured F via the Luttinger rule, $x = 1 - (2eFa^2/h)$, are listed in Table S3 below.

Section 2

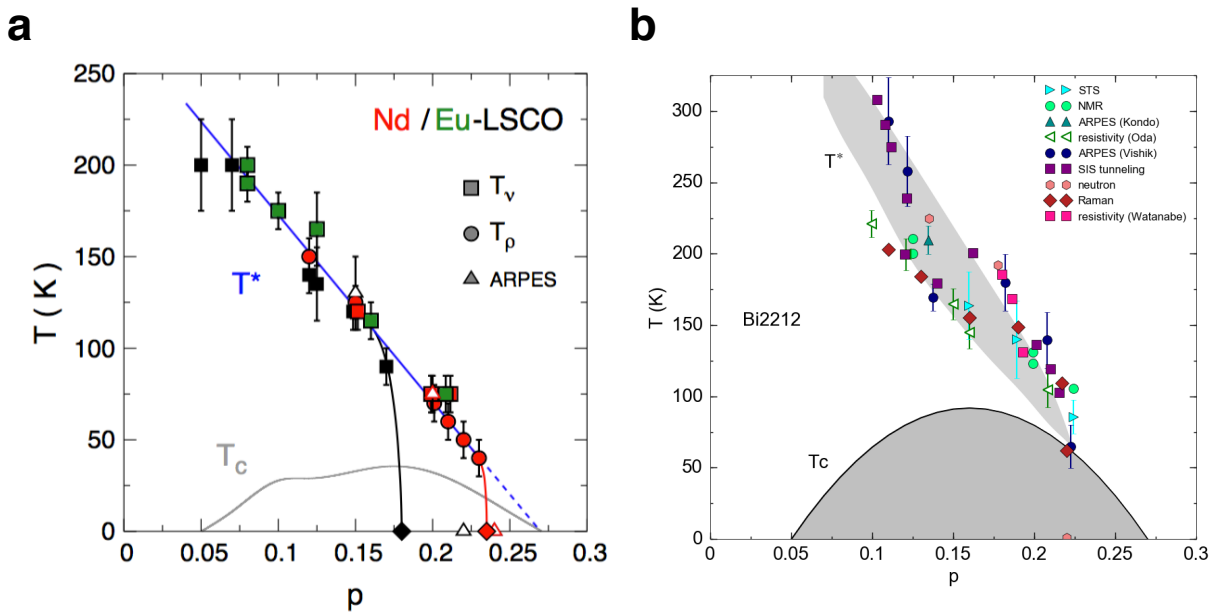

Figure S2 | Phase diagram of hole-doped cuprates.

Temperature-doping phase diagrams: **(a)** Nd-LSCO (red) and LSCO (black) (from ref. 45); **(b)** Bi2212 (adapted from ref. 46, neutron data come from ref. 47, Raman data from ref. 22 and *c*-axis resistivity data from ref. 48). The pseudogap phase ends at the critical doping $p^* = 0.23$ in Nd-LSCO, $p^* = 0.18$-0.19 in LSCO, and $p^* = 0.22$ in Bi2212.

Section 3

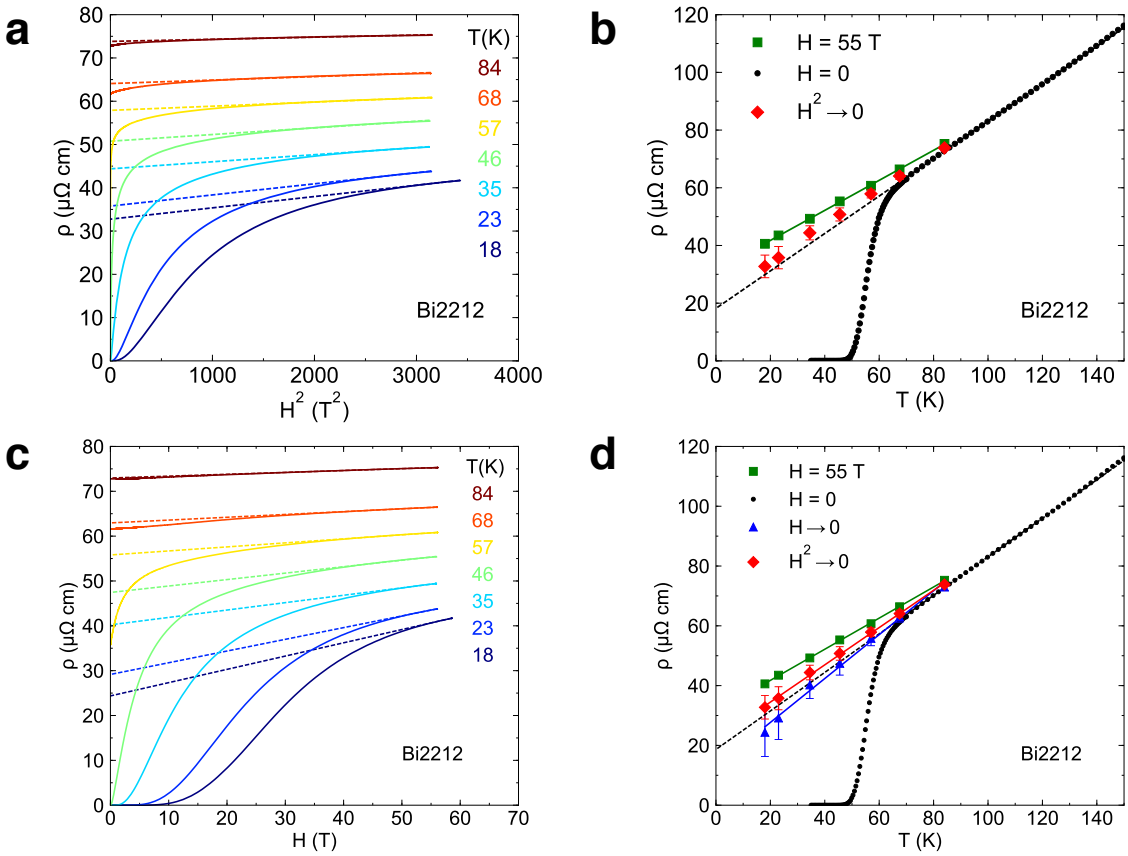

Figure S3 | Correcting for the magneto-resistance in Bi2212.

a) Magnetic field dependence of the resistivity ρ in our sample of Bi2212, plotted vs H^2, at different temperatures as indicated. The dashed lines are linear fits to the data at high H, *i.e.* $\rho(H) = \rho(H^2 \rightarrow 0) + cH^2$. **b)** Temperature dependence of ρ: at H = 0 (black dots), at H = 55 T (green squares), and $\rho(H^2 \rightarrow 0)$ (red diamonds) obtained from the fits in panel a). The error bars on the back-extrapolated $H^2 \rightarrow 0$ values are estimated as being $[\rho(H = 55\ \mathrm{T}) - \rho(H^2 \rightarrow 0)] / 2$. The green line is a linear fit to ρ(55T); the dashed black line a linear fit to the H = 0 data between 80 K and 130 K. **c)** Magnetic field dependence of the resistivity ρ in Bi2212 at different temperatures. The dashed lines are a linear fit to the data at high H, over the same field ranges as in panel a). **d)** Same as panel b) but including the value of the resistivity back extrapolated to H = 0 with the linear fits shown in panel c) (blue triangles). The error bar on the blue triangles grows as the fit range decreases.

In Fig. 2a, isotherms in Bi2212 exhibit a small normal-state magnetoresistance (MR). In Fig. S3a, we see that this MR grows as H^2, at T = 84 K. To correct for the MR at lower T, we fit the data to $\rho(H) = \rho(H^2 \rightarrow 0) + cH^2$ above a threshold field (dashed lines in Fig. S3a), namely : 40 T for T = 68, 57 and 46 K; 50 T for T = 35 and 23 K; 55 T for T = 18 K. In Fig. S3b, we plot $\rho(H^2 \rightarrow 0)$ vs T (red diamonds) and observe that $\rho(H^2 \rightarrow 0)$ is the linear continuation (dashed line) of the H = 0 data at high T (black dots), within error bars. This shows that in the absence of MR, the normal-state resistivity of Bi2212 is T-linear from T ~ 120 K down to at least T = 18 K. The slope of $\rho(H^2 \rightarrow 0)$ vs T (red diamonds, Figs. 2b and S3b) is A_1 = 0.62 μΩ cm / K (Table S2 below), while the slope of $\rho(H$=55T) vs T (red squares, Fig. 1a) is A_1 = 0.50 μΩ cm / K. Note that the same approach was used to correct for the MR in LSCO (see ref. 8). Motivated by the recent claim of linear magnetoresistance at the quantum critical point of LSCO (ref. 49), we show in Fig. S3c a linear fit of the magnetoresistance using the same field ranges as in panel a). In Fig. S3d, we compare the temperature dependence of the resistivity using linear (blue triangles) and quadratic (red diamonds) back extrapolation of the magnetoresistance. We see that the two methods agree within error bars, and both are consistent with the simple linear extension of the zero-field $\rho(T)$ curve.

Section 4

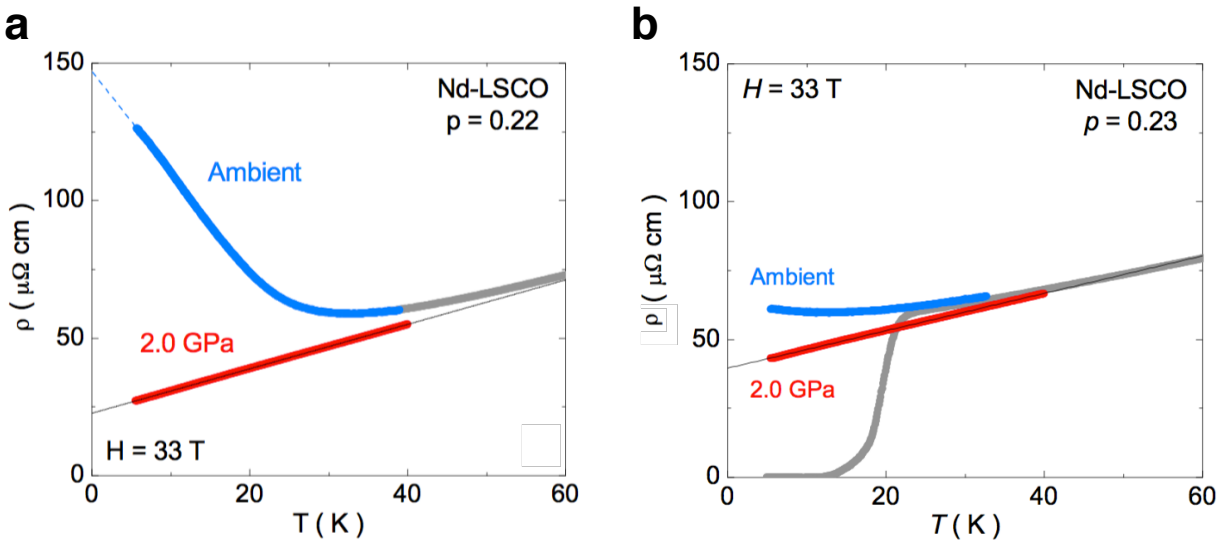

Figure S4 | Resistivity of Nd-LSCO under pressure.

Normal-state resistivity of Nd-LSCO at p = 0.22 (**a**) and p = 0.23 (**b**), measured at H = 0 (grey) and H = 33 T at ambient pressure (blue) and at P = 2.0 GPa (red) (from ref. 12). The effect of pressure is to suppress the pseudogap phase, by moving p^* below 0.22. This shows that the resistivity is then perfectly linear at low T.

T-linear resistivity in Nd-LSCO was first reported in 2009, at p = 0.24 (ref. 7). At lower doping, the resistivity shows an upturn at low T, the signature of the pseudogap (refs. 7, 11). This yields p^* = 0.23 in Nd-LSCO (ref. 11), consistent with ARPES data that find the pseudogap in Nd-LSCO to close at a doping above p = 0.20 and below p = 0.24 (ref. 19).

It was recently found that p^* can be lowered by the application of hydrostatic pressure (ref. 12). A pressure of 2 GPa moves p^* below 0.22, *i.e.* it removes the resistivity upturn in Nd-LSCO at p = 0.22 and p = 0.23 (Fig. S4). Having removed the pseudogap, one finds a perfectly linear T dependence as $T \rightarrow 0$ (Fig. S4). We then see that the regime of T-linear resistivity is stretched from p = 0.24 down to p^*, producing an anomalous range similar to that found in LSCO (ref. 8). In that range, we again observe that A_1 increases with decreasing p (Figs. 1c and 3b).

Section 5

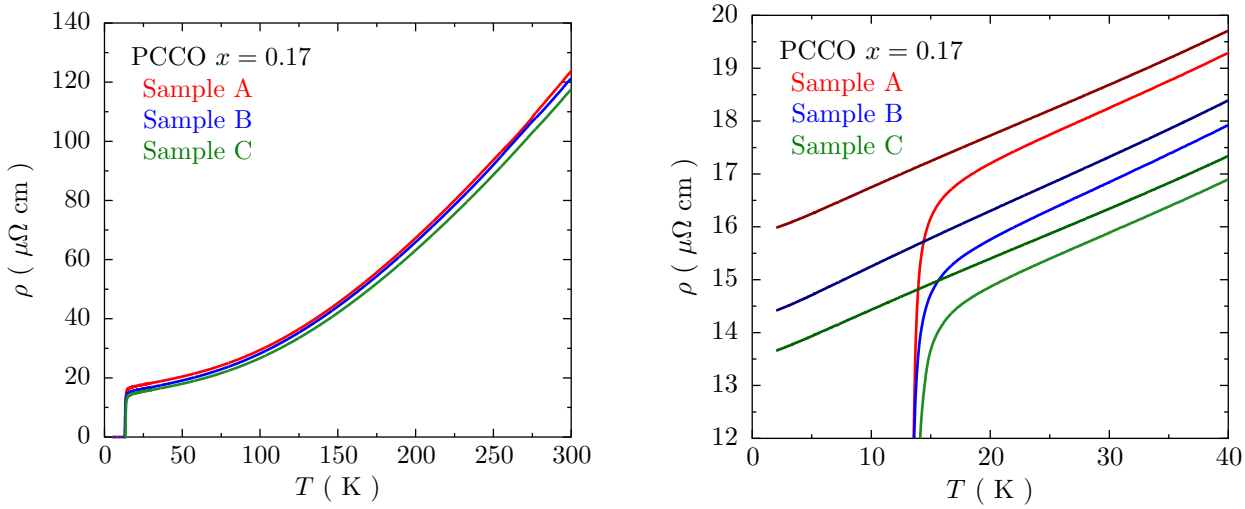

Figure S5 | Resistivity of our PCCO films.

a) Temperature dependence of the resistivity in our three PCCO films with x = 0.17, in zero field. **b)** Zoom on the low-temperature regime, at H = 0 (pale) and H = 16 T (dark). The 16 T curve for sample C is also shown in Fig. 1d.

To double-check the value of A_1 in PCCO at x = 0.17, we have grown and measured three films of PCCO at x = 0.17, with T_c = 13.1 K (sample A), 13.0 K (sample B) and 13.4 K (sample C). These films have a very similar residual resistivity ratio, RRR = ρ(300K)/ρ(T→0) = 8.2, 8.8 and 9.1, respectively. The sample thickness t = 230 ± 30 um is measured by the width of the x-ray diffraction peak. For films of that thickness, the uncertainty is roughly ± 15%. As shown in Fig. S5, we obtain A_1 = 0.10 μΩ cm / K on all three films (at H = 0), in good agreement with published data. Applying a field of 16 T suppresses superconductivity completely (H_{c2} = 3 T; ref. 17) and extends the linear T dependence to the lowest T. The slope at H = 16 T is the same as in zero field (see Table S4 below). We conclude that $A_1^{\square}$ = 1.7 ± 0.3 Ω / K in PCCO at x = 0.17 (Fig. 4b and Table 1).

Section 6

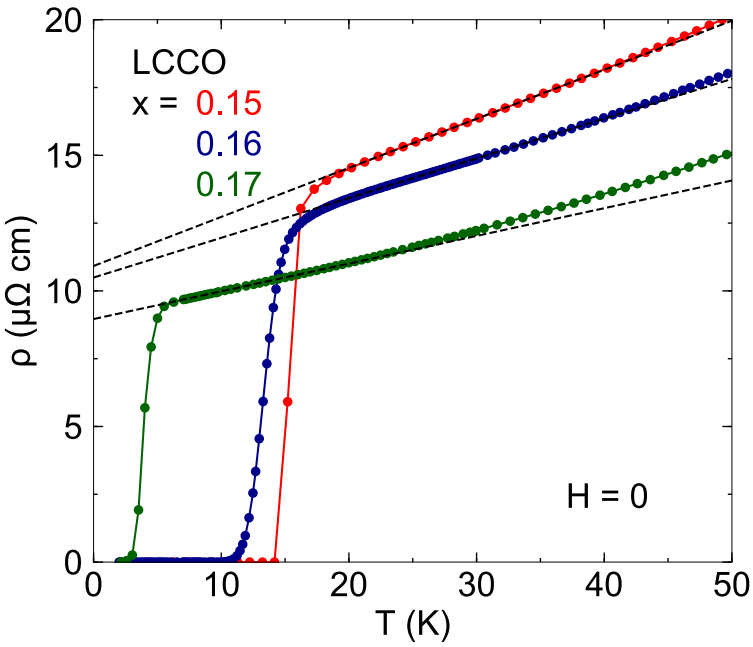

Figure S6 | Resistivity of LCCO films.

Temperature dependence of the resistivity in LCCO in zero field at three dopings, as indicated (from ref. 14, and courtesy of R.L. Greene). Lines are a linear fit to low-*T* data.

In electron-doped cuprates, *T*-linear resistivity was first observed in PCCO at x = 0.17 in 1998 (ref. 2). At the time, thin films contained traces of an extra phase, and so the absolute value of the resistivity was not reliable. Since 2009 (ref. 41), this has been resolved. In recent measurements on PCCO (refs. 17,41) and on LCCO (refs. 13,14), a *T*-linear resistivity at low *T* with reliable absolute value has been reported, giving A_1 = 0.1 μΩ cm / K in both PCCO and LCCO at x = 0.17 (Table S4).

In Fig. S6, we reproduce the zero-field resistivity of LCCO at x = 0.15, 0.16 and 0.17, from ref. 14 (and courtesy of R. L. Greene). Linear fits at low *T* yield the values of A_1 listed in Table S4 below, which give A_1 = 3.0, 2.4 and 1.7 Ω / K at x = 0.15, 0.16 and 0.17, respectively.

In Fig. 1d, we reproduce the in-field resistivity of LCCO at x = 0.15, 0.16 and 0.17, from ref. 14 (and courtesy of R. L. Greene). Linear fits at low *T* yield values of A_1 that are very similar to the zero-field values (see Table S4 below).

Section 7

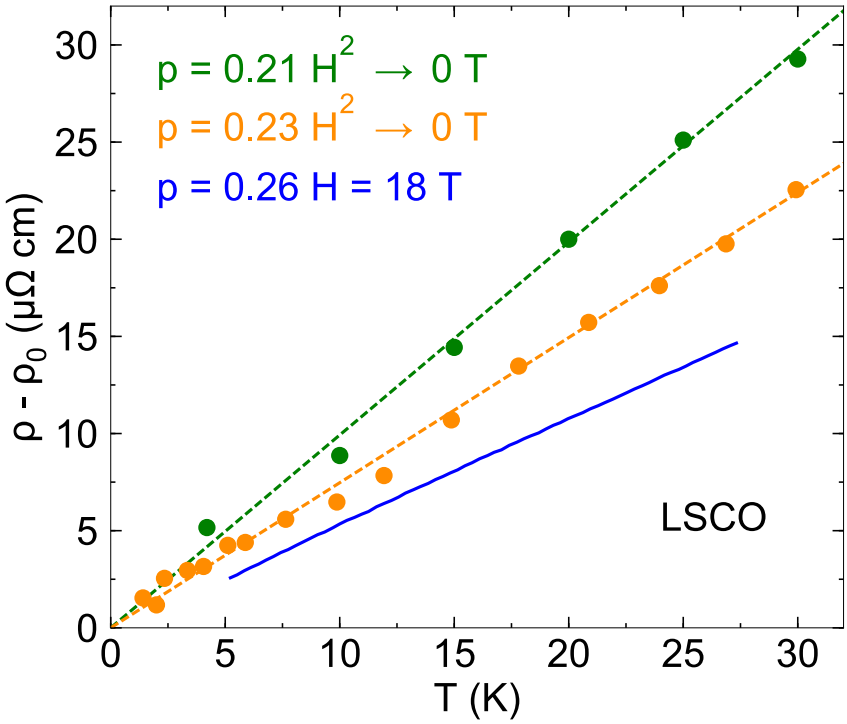

Figure S7 | Resistivity of LSCO corrected for MR.

Temperature-dependent part of the normal-state resistivity of LSCO, $\rho(T) - \rho_0$, at p = 0.21 (green) and p = 0.23 (orange), from ref. 8, and at p = 0.26 (blue, H = 18 T; from ref. 42). The green and orange dots are the MR-corrected resistivity, $\rho(H^2 \rightarrow 0)$, obtained in ref. 8 from a fit of ρ vs H isotherms to $\rho(H) = \rho(H^2 \rightarrow 0) + cH^2$. The green and orange lines are a linear fit to $\rho(H^2 \rightarrow 0)$ vs T, whose slope A_1 is given in Table S2 below.

The low-T resistivity of LSCO was measured by Cooper *et al*. from p = 0.18 up to p = 0.33, by applying a magnetic field up to 60 T (ref. 8). At p = 0.21, 0.23 and 0.26, 48 T is sufficient to suppress superconductivity down to (at least) 2 K. At those three dopings, the resistivity is linear as $T \rightarrow 0$, below a certain temperature T_0. At p = 0.23, for example, a perfect linearity is observed in the raw data at 48 T below 50 K (down to at least 2 K). The slope A_1 in 48 T is the same as the slope in zero field observed between T_c and T_0 ~ 75 K. At p = 0.21, T_0 ~ 150 K, while at p = 0.26,

T_0 ~ 30 K (ref. 42). The value of A_1 increases with decreasing p (Fig. 1b, Fig. 3b). At $p > 0.26$, the resistivity is no longer purely T-linear at low T. Instead, it can be fit to $A_1 T + A_2 T^2$ at $p = 0.29$ and to $A_2 T^2$ at $p = 0.33$ (*i.e.* $A_1 = 0$). So the T-linear resistivity as $T \rightarrow 0$ is observed in LSCO from $p = 0.26$ down to at least $p = 0.21$, possibly down to $p = 0.18$ (where it is more difficult to suppress superconductivity), *i.e.* down to p^* ~ 0.18-0.19. In LSCO, p^* is identified as the doping below which the resistivity is no longer T-linear at low T, and $p^* = 0.18$-0.19 is consistent with ARPES data that find the pseudogap in LSCO to close above $p = 0.15$ and below $p = 0.22$ (ref. 20). The fact that T-linear resistivity is observed over a sizable range of doping is considered anomalous and requires an explanation.

Section 8

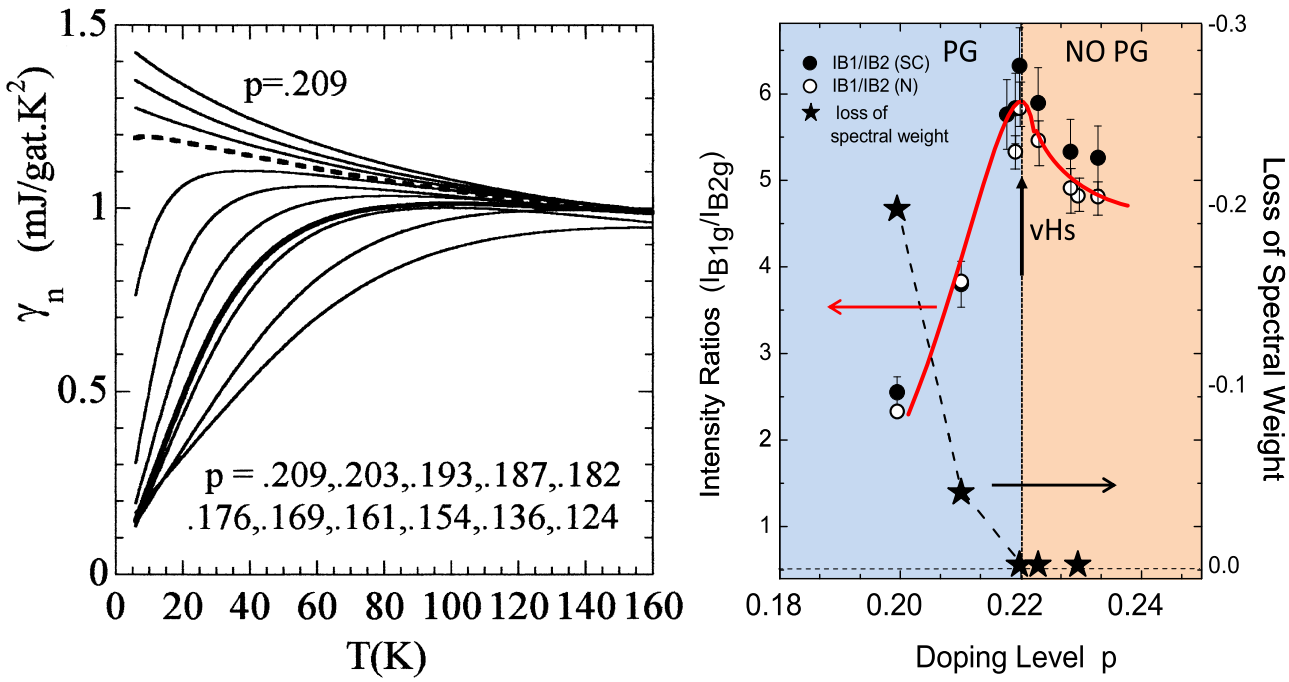

Figure S8 | Specific heat and Raman intensity in Bi2212.

a) Normal-state specific heat coefficient γ of Bi2212 vs temperature, at various dopings as indicated, estimated from an analysis of data up to high temperature (from ref. 33). **b)** Ratio of Raman intensities in Bi2212 vs doping, for the modes that select anti-nodal (B_{1g}) vs nodal (B_{2g}) regions in *k*-space (from ref. 22).

In the T = 0 limit, γ in Bi2212 is seen to increase from 1.2 at p = 0.187 to 1.5 mJ / gat. K^2 at p = 0.209. A linear extrapolation up to p = 0.22 yields γ = 1.65 ± 0.15 mJ / gat. K^2 at p = 0.22, which converts to γ = 12 ± 2 mJ / K^2 mol-Cu (Table S1 below). The peak in the Raman intensity ratio, which is sensitive to the opening of the anti-nodal pseudogap (PG), shows that the pseudogap critical point in Bi2212 is p^* = 0.22. Our sample has a doping of p = 0.23, and so is very slightly above p^*. It is reasonable to assume that γ at T = 0 (panel a) will continue to increase until p reaches p^*.

Section 9

Planckian limit in the organic conductors

The organic conductor $(TMTSF)_2PF_6$ is a well-characterized single-band metal. When tuned to its QCP (by pressure), $(TMTSF)_2PF_6$ exhibits a resistivity that is perfectly *T*-linear below 8 K, down to the lowest measured temperature (~ 0.1 K), with a slope A_1 = 0.38 ± 0.04 μΩ cm / K (ref. 4). With a carrier density $n = 1.4\times10^{27}$ m^{-3} (ref. 50) and an effective mass $m^* = 1.0 – 1.3\ m_0$ (ref. 51), we get $A_1 = \alpha\ (m^* / n)\ (k_B / e^2 \hbar) = \alpha$ (0.33 – 0.43 μΩ cm / K), so that α = 1.0 ± 0.3 (Table 1).

To calculate the 2D sheet resistance listed in Table 1, we divide A_1 by the interlayer separation along the *c* axis, *d* = 1.35 nm, yielding $A_1^{\square} = A_1 / d$ = 2.8 ± 0.3 Ω / K.

Section 10

Planckian limit in the single-layer cuprate Bi2201

In the single-layer cuprate Bi2201, the pseudogap critical point is located at very high doping, near the end of the superconducting dome, namely where T_c ~ 10 K [52]. The Fermi surface measured by ARPES is also found to change topology from hole-like to electron-like near the end of the superconducting dome [53]. The volume of the Fermi surface at that doping is such that *p* ~ 0.4 [53], so that the carrier density contained in the electron-like Fermi surface is $n = 1 – p$ ~ 0.6.

Near the end of the superconducting dome, at T_c ~ 7 K, the resistivity is found to be perfectly *T*-linear [6]. In two crystals with nearly the same doping (T_c), A_1 = 0.74 and 1.06 μΩ cm / K [6]. Taking the average of those two values, consistent with typical error bars on geometric factors (±15%), we get A_1 = 0.9 ± 0.2 μΩ cm / K. Dividing by the interlayer spacing, which is two times larger in Bi2201 than in LSCO, we get $A_1^{\square}$ = 8 ± 2 Ω / K. Remarkably, this is the same value, within error bars, as in Bi2212 and Nd-LSCO, all at their respective critical dopings, namely p^* = 0.22, 0.23, and 0.4 (Table 1).

We can estimate m^* from specific heat data measured on a Bi2201 crystal with T_c = 19 K [54], at a doping slightly below p^* [52]. With increasing field to suppress superconductivity, γ increases from 6 mJ / K^2 mol at *H* = 0 to 8 mJ / K^2 mol at *H* = 6 T, and is estimated to reach 10 mJ / K^2 mol at the critical field H_{c2} = 18 T [54]. Given the uncertainty in the latter estimation, we take

$\gamma = 10 \pm 2$ mJ / K^2 mol , which yields $m^* = 7 \pm 1.5\ m_0$. Note that γ may be somewhat larger at the slightly higher doping ($p \sim p^*$) where T-linear resistivity was measured (see Supplementary Section 8 for a similar situation with respect to the specific heat data in Bi2212.)

Using $n = 0.6$ and $m^* = 7 \pm 1.5\ m_0$, we calculate the value predicted for the Planckian limit: $A_1^{\square} = (m^* / n\ d)\ (k_B / e^2\ \hbar) = 8 \pm 2\ \Omega$ / K. The ratio of experimentally measured to theoretically predicted values of $A_1^{\square}$ is therefore $\alpha = 1.0 \pm 0.4$ (Table 1).

Section 11

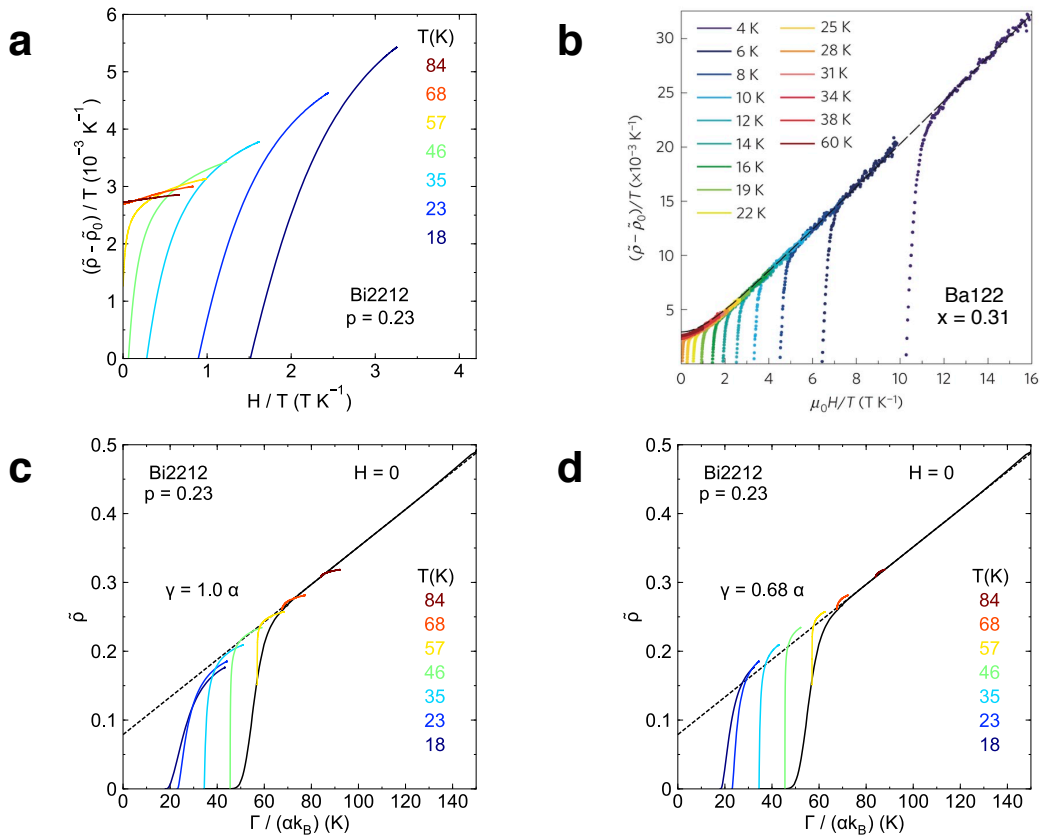

Figure S9 | *H-T* scaling in Bi2212 at *p* = 0.23.

a) Resistivity of Bi2212 at p = 0.23 normalized at 300 K, plotted as a function of H / T, at different temperatures. **b)** Same plot as in panel a) but for the compound $BaFe_2(As_{1-X}P_x)_2$ at x = 0.31 (from ref. 27). **c)** Resistivity of Bi2212 at p = 0.23, normalized at 300 K, plotted as a function of the energy scale Γ (defined in Eq. S1) divided by α k_B. The black solid line corresponds to zero-field data and the curves in colour refer to the pulsed-field isotherms. The dotted black line is a linear fit to zero-field data between 80 K and 130 K. At zero field, Γ / α k_B is simply equal to T. When $H \neq 0$, Γ / α k_B is given by the quadrature sum of temperature and applied field modulo the ratio γ / α (see Eq. S1). In this panel, γ / α = 1, as in panel b (ref. 27). **d)** Same as in panel c), but with γ / α = 0.68, obtained by assuming a linear magnetoresistance at T = 18 K (see Fig. S3c).

Scaling between magnetic field and temperature

Near the quantum critical point of the iron-based superconductor $BaFe_2(As_{1-X}P_x)_2$, at x = 0.31, Hayes *et al.* highlighted a specific scaling between temperature and magnetic field dependences of the resistivity [27]. Indeed, the resistivity looks linear both in temperature and in magnetic field. By plotting the temperature dependence of the resistivity (normalized at room temperature), divided by T, as a function of H / T, all the isotherms fall on the same curve in the normal state (Fig. S9b). This led Hayes *et al.* to suggest the following ansatz for the (T, H) dependence of the resistivity at the quantum critical point of $BaFe_2(As_{1-X}P_x)_2$:

$$\rho\,(H,T) - \rho(0,0) \propto [(\alpha\, k_B\, T)^2 + (\gamma\, \mu_B\, \mu_0\, H)^2)]^{1/2} \equiv \Gamma\,, \qquad \text{(S1)}$$

where Γ is a new energy scale, and α and γ are dimensionless parameters that can be obtained from the linear slope of the resistivity at zero field above T_c and from the linear slope of the magnetoresistance as $T \rightarrow 0$, respectively. If we perform the same analysis in Bi2212 at p = 0.23 (Fig. S9a), we notice that the isotherms do not lie on the same curve in the normal state, unlike in $BaFe_2(As_{1-X}P_x)_2$. This may simply be explained by the fact that the magneto-resistance is not purely linear in this sample (see Section 3).

The disagreement with the scaling of Hayes *et al*. for Bi2212 is confirmed by plotting the normalized resistivity as a function of Γ / (k_B T) (Figs. S9c and S9d). If we take the same ratio, γ / α = 1, as in ref. 27 (Fig. S9b), we do not observe in Bi2212 (Fig. S9c) that the isotherms asymptotically approach a single line that would be the extrapolated T-linear resistivity above T_c. Assuming that the magnetoresistance is linear in field at the lowest temperature (see Fig. 3c), we obtain γ / α = 0.68. Fig. S9d displays the resistance of Bi2212 as a function of Γ with this ratio, and we see that the scaling does not work very well.

In conclusion, the empirical scaling between magnetic field and temperature found close to the quantum critical point in $BaFe_2(As_{1-X}P_x)_2$ does not appear to work in Bi2212. (Giraldo-Gallo *et al*. recently showed that the resistivity of LSCO at p = 0.19, near the critical doping, behaves linearly as a function of field and temperature, but they didn't show any scaling relation [49].)

Section 12

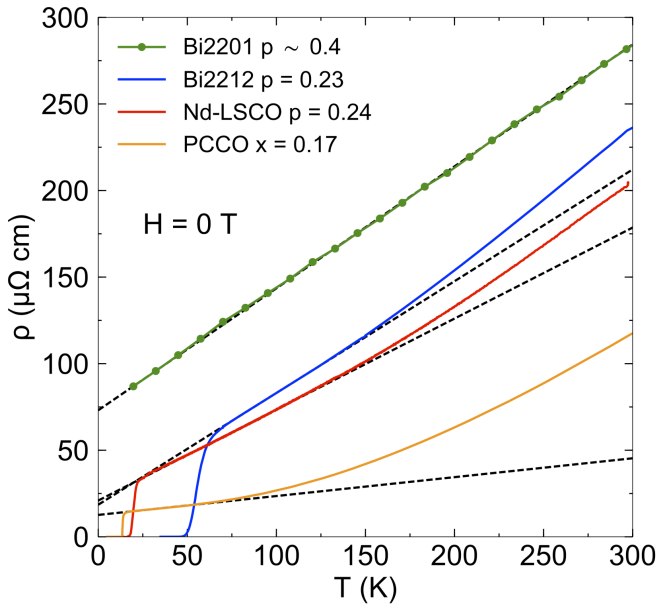

Figure S10 | Resistivity vs temperature for various cuprates near their critical point.

Resistivity as a function of temperature for different cuprates, in zero field: Bi2201 at $p \approx 0.4$ (green; ref. 6); Bi2212 at $p = 0.23$ (blue; this work); Nd-LSCO at $p = 0.24$ (red; ref. 11); PCCO at x = 0.17 (orange; this work). The black dotted lines are linear fits of the data just above T_c.

Temperature range of *T*-linear resistivity

In this paper, our focus has been on the *T*-linear resistivity in the low *T* limit. The question of how high in temperature the *T*-linear regime extends is an interesting one, to which there is no clear answer at present. As seen in Fig. S10, in some cuprates that range is short (limited below ~ 50 K in PCCO) while in other cuprates it is very long (beyond 300 K in Bi2201). As shown for LSCO in ref. 8, the range does appear to stretch as the system gets closer to its p^*: at $p = 0.23$, the *T*-linear regime is limited to $T < 80$ K or so, while at $p = 0.19$, it extends up to $T \sim 300$ K (see also ref. 49).

Section 13

Tables

Material	p	γ (mJ / K^2 mol)	m^* / m_0	Ref.	$h / (2e^2 T_F)$ (Ω / K)
Bi2212	0.22	12 ± 2	8.4 ± 1.6	33	7.4 ± 1.4
LSCO	0.26 ± 0.005	14 ± 2	9.8 ± 1.7	35	8.9 ± 1.8
	0.29 ± 0.01	11 ± 1	7.7 ± 0.9	35	7.3 ± 1.2
	0.33 ± 0.01	6.9 ± 1	4.8 ± 0.8	34	4.9 ± 1.0
Nd-LSCO	0.24 ± 0.005	17 ± 5	12 ± 4	36	10.6 ± 3.7
	0.27 ± 0.01	11 ± 1	7.7 ± 0.9	36	7.1 ± 1.1
	0.36 ± 0.01	6.2 ± 1	4.3 ± 0.8	36	4.6 ± 1.0
	0.40 ± 0.01	5.4 ± 1	3.8 ± 0.8	36	4.2 ± 1.1

Table S1 | Effective mass and Planckian limit estimates in hole-doped cuprates.

Values of p and m^* used in Fig. 3a and described in the text and Methods. The effective mass m^* is obtained from the measured specific heat γ via Eq. 2, except for Nd-LSCO p = 0.24. At this doping, C_e / T is not constant at low T (ref. 36). Therefore, we take the average between C_e / T at T = 10 K (12 mJ / K^2 mol) and at T = 0.5 K (22 mJ / K^2 mol) as representative of the residual γ, with appropriate error bars. The last column shows the Planckian limit prediction for the resistivity slope $A_1^{\square} = h / (2e^2 T_F)$, calculated using p and m^* values. Error bars are explained in the Methods.

Material	p	A_1 ($\mu\Omega$ cm / K)	d (Å)	$A_1^{\square}$ (Ω / K)	H (T)	Ref.
Bi2212	0.23	0.62 ± 0.06	7.73 ± 0.05	8.0 ± 0.9	→ 0	this work
LSCO	0.21 ± 0.005	1.0 ± 0.09	6.57 ± 0.05	15.2 ± 1.5	→ 0	8
	0.23 ± 0.005	0.75 ± 0.08	6.57 ± 0.05	11.4 ± 1.3	→ 0	8
	0.26 ± 0.005	0.54 ± 0.06	6.57 ± 0.05	8.2 ± 1.0	18	42
Nd-LSCO	0.22 ± 0.003	0.81 ± 0.08	6.64 ± 0.05	12.2 ± 1.3	33	12
	0.23 ± 0.003	0.68 ± 0.07	6.64 ± 0.05	10.2 ± 1.1	33	12
	0.24 ± 0.005	0.49 ± 0.05	6.64 ± 0.05	7.4 ± 0.8	16	7, 11

Table S2 | Slope of *T*-linear resistivity in hole-doped cuprates.

Values of p and A_1 described in the text and Methods. The interlayer distance d is given, yielding the experimental values $A_1^{\square} = A_1 / d$ that are plotted in Fig. 3b. Error bars are explained in the Methods.

Material	x	γ (mJ / K^2 mol)	m^* / m_0	Ref.	$h / (2e^2 T_F)$ (Ω / K)
PCCO	0.15 ± 0.005	5.5 ± 0.4	3.6 ± 0.3	31	3.1 ± 0.3
NCCO	0.151	-	3.0 ± 0.3	29, 30	2.6 ± 0.3
	0.157	-	2.7 ± 0.1	29, 30	2.35 ± 0.1
	0.163	-	2.5 ± 0.1	29, 30	2.2 ± 0.1
	0.173	-	2.3 ± 0.05	29, 30	2.05 ± 0.05

Table S3 | Effective mass and Planckian limit estimates in electron-doped cuprates.

Values of x and m^* used in Fig. 4a and described in the text and Methods. The effective mass m^* was measured directly using quantum oscillations in NCCO (refs. 29, 30) and using specific heat γ in PCCO (ref. 31). The last column shows the Planckian limit prediction for the resistivity slope, calculated using x and m^* values. Error bars are explained in the Methods.

Material	x	A_1 ($\mu\Omega$ cm / K)	d (Å)	$A_1^{\square}$ (Ω / K)	H (T)	Ref.
PCCO	0.17 ± 0.005	0.10 ± 0.015	6.07 ± 0.05	1.7 ± 0.3	0	this work
		0.10 ± 0.015	6.07 ± 0.05	1.7 ± 0.3	16	this work
LCCO	0.15 ± 0.005	0.18 ± 0.03	6.20 ± 0.05	3.0 ± 0.45	0	14
		0.18 ± 0.03	6.20 ± 0.05	3.0 ± 0.45	8	14
	0.16 ± 0.005	0.145 ± 0.02	6.20 ± 0.05	2.4 ± 0.35	0	14
		0.12 ± 0.02	6.20 ± 0.05	1.9 ± 0.3	6.5	14
	0.17 ± 0.005	0.10 ± 0.015	6.20 ± 0.05	1.7 ± 0.3	0	14
		0.09 ± 0.015	6.20 ± 0.05	1.5 ± 0.2	4	*

* Courtesy of R. L. Greene.

Table S4 | Slope of *T*-linear resistivity in electron-doped cuprates.

Values of x and A_1 described in the text and Methods. The interlayer distance d is given, yielding the experimental values $A_1^{\square} = A_1 / d$ that are plotted in Fig.4b. Error bars are explained in the Methods.

SUPPLEMENTARY REFERENCES

[44] Helm, T. Electronic properties of electron-doped cuprate superconductors probed by high-field magneto-transport. *PhD thesis*. Technical University, Munich (2013).

[45] Cyr-Choinière, O. *et al.* Pseudogap temperature *T** of cuprates from the Nernst effect. *Phys. Rev. B* **97**, 064502 (2018).

[46] Vishik, I. M. *et al.* Phase competition in trisected superconducting dome. *PNAS* **109**, 18332-18337 (2012).

[47] Mangin-Thro, L. *et al.* Characterization of the intra-unit-cell magnetic order in $Bi_2Sr_2CaCu_2O_{8+\delta}$. *Phys. Rev. B* **89**, 094523 (2014).

[48] Watanabe, T., Fujii, T. & Matsuda, A. Pseudogap in $Bi_2Sr_2CaCu_2O_{8+\delta}$ studied by measuring anisotropic susceptibilities and out-of-plane transport. *Phys. Rev. Lett.* **84**, 5848–5851 (2000).

[49] Giraldo-Gallo, P. *et al.* Scale-invariant magnetoresistance in a cuprate superconductor. Science **361**, 479-481 (2018).

[50] Moser, J. *et al*. Hall effect in the normal phase of the organic superconductor $(TMTSF)_2PF_6$. *Phys. Rev. Lett.* **84**, 2674-2677 (2000).

[51] Uji, S. *et al*. Rapid oscillations and Fermi-surface reconstruction due to spin-density-wave formation in the organic conductor $(TMTSF)_2PF_6$. *Phys. Rev. B* **55**, 12446-12453 (1997).

[52] Kawasaki, S. *et al.* Carrier-concentration dependence of the pseudogap ground state of superconducting $Bi_2Sr_{2-x}La_xCuO_{6+\delta}$ revealed by ^{63,65}Cu-nuclear magnetic resonance in very high magnetic fields. *Phys. Rev. Lett.* **105**, 137002 (2010).

[53] Kondo, T. *et al.* Hole-concentration dependence of band structure in $(Bi,Pb)_2(Sr,La)_2CuO_{6+\delta}$ determined by the angle-resolved photoemission spectroscopy. *J. Electron Spectroscopy and Related Phenomena* **137-140**, 663-668 (2004).

[54] Ikuta, H. *et al.* Low-temperature specific heat of overdoped Bi2201 single crystals. *Physica C* **388-389**, 361-362 (2003).